water

MDPI

Supplementary Material

Hydrogeochemical Variability of the Acidic Springs in the Rio Tinto Headwaters

Christopher John Allman [1], David Gómez-Ortiz [2], Andrea Burke [3], Ricardo Amils [4,5], Nuria Rodriguez [5] and David Fernández-Remolar [6,7,*]

[1] Beca Limited, 32 Harington Street, Tauranga 3110, New Zealand; Christopher.Allman@beca.com
[2] ESCET-Área de Geología, Universidad Rey Juan Carlos, 28933 Móstoles, Spain; david.gomez@urjc.es
[3] School of Earth & Environmental Sciences, University of St Andrews, St Andrews KY16 9AJ, UK; ab276@st-andrews.ac.uk
[4] Centro de Biología Molecular Severo Ochoa (CSIC-UAM), Universidad Autónoma de Madrid, 28049 Madrid, Spain; ramils@cbm.csic.es
[5] Centro de Astrobiología (CSIC-INTA), 28850 Torrejón de Ardoz, Spain; nrodriguez@cbm.csic.es
[6] State Key Laboratory of Lunar and Planetary Sciences, Macau University of Science and Technology, Macau 999078, China
[7] CNSA Macau Center for Space Exploration and Science, Macau 999078, China
* Correspondence: dcfremolar@must.edu.mo

Supplementary File

Contents: Figures S1 to S6, and Tables S1 to S4

1. Supplemental Figures

Figure S1. Simplified geological map of the study area showing the different lithologies, structures and sampling locations.

Figure S2. ERT (Electric Resistivity Tomography) sounding results for profiles 1 and 2 showing the underground lithological and tectonic structure (for more information see Gómez-Ortiz et al. (2014) Identification of the subsurface sulfide bodies responsible for acidity in Río Tinto source water, Spain. Earth and Planetary Science Letters, 391, 36–41. doi:http://dx.doi.org/10.1016/j.epsl.2014.01.022).

Figure S3. A GIS diagram displaying proportional symbols which represent the total cations from each of the springs.

Figure S4. GIS diagram of the study area, with proportional symbols representing concentrations of specific elements in mg/L as aluminium (a), cobalt (b), calcium (c), manganese (d), zinc (e), and iron (f).

Figure S5. Different GIS maps which representing the total anion composition (a), Sulfate (b), phosphate (c), and fluorine (d) for each locality in a proportional symbology format.

Figure S6. Rainwater and spring $\delta^{18}O$ and $\delta^{2}H$ in the study area. a) $\delta^{18}O$ values for the Rio Tinto springs, with the average $\delta^{18}O$ value for the rainwater on the 24/06/2014 and data from GNIP spanning 2000–2006; b) $\delta^{2}H$ values for the Rio Tinto springs with an average $\delta^{2}H$ value for the rain collected on the 24/06/2014 and an average of GNIP data from 2000–2006.

2. Supplemental Tables

Table S1. Tables summarizing the accuracy of the isotopic analysis in relation to the standards, IA-RO52, IA-RO53 and IA-RO54, and the standards used in the isotopic analysis.

Table S2. Rainwater average isotope data 2000-2006 for Seville. Weighted values are used to correct biases in the 2H concentration by re-evaporation processes (see Hughes, C. E. and Crawford, J. (2012). A new precipitation weighted method for determining the meteoric water line for hydrological applications demonstrated using Australian and global GNIP data. Journal of Hydrology, 464–465, 344351. doi:https://doi.org/10.1016/j.jhydrol.2012.07.029).

Table S3. Table summarizing the acid producing minerals within the VSC deposit of Rio Tinto and the acidity of each, complemented by their reaction rates through Fe^{3+} (Dold, 2010).

Table S4. Summarizing the PHREEQC results, with N/A assuming the mineral does not form under those conditions or that the elements are in large enough concentrations to form sufficient mineral. Standard state conditions were used within the input file.

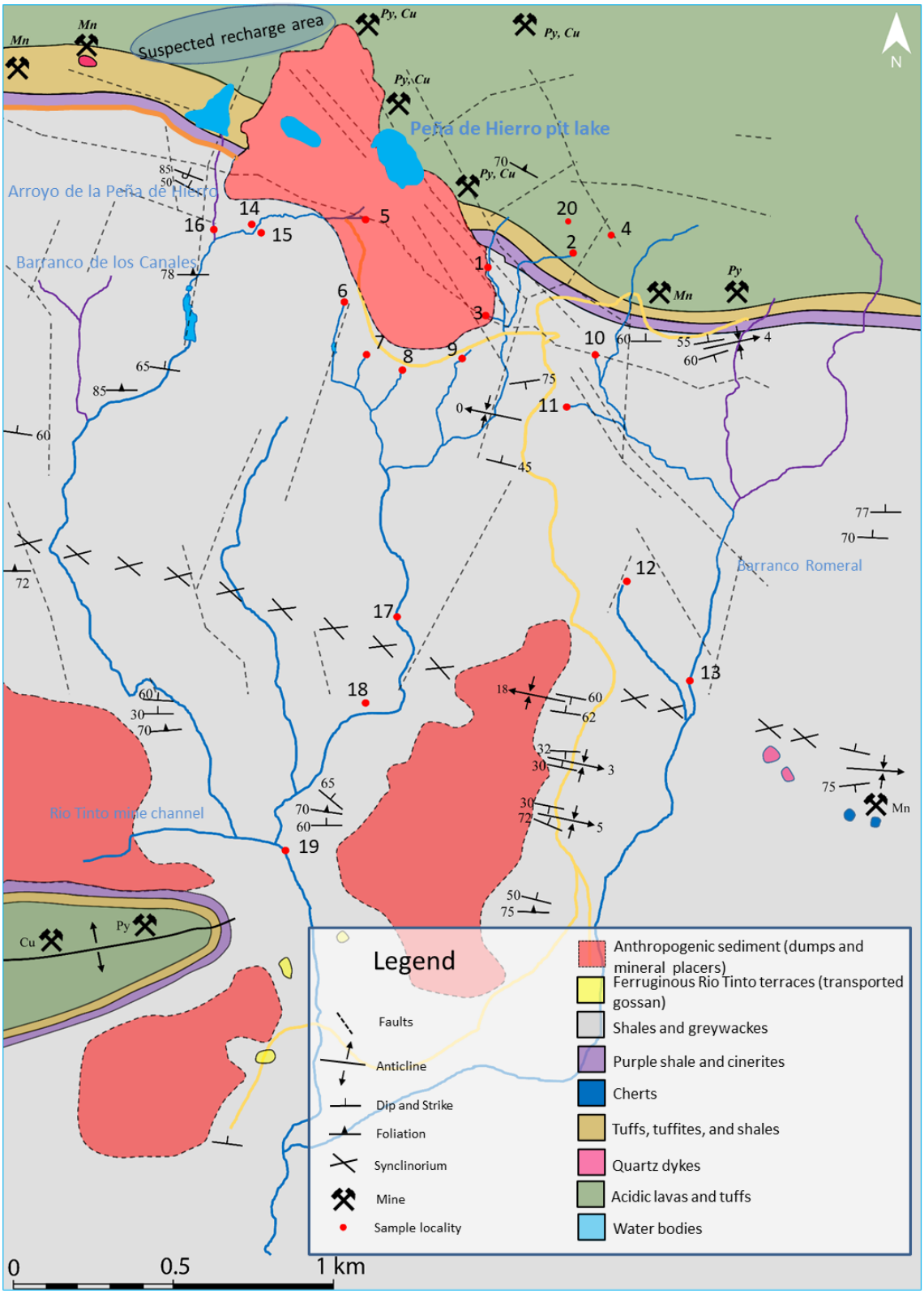


Figure S1. Simplified geological map of the study area showing the different lithologies, structures and sampling locations.

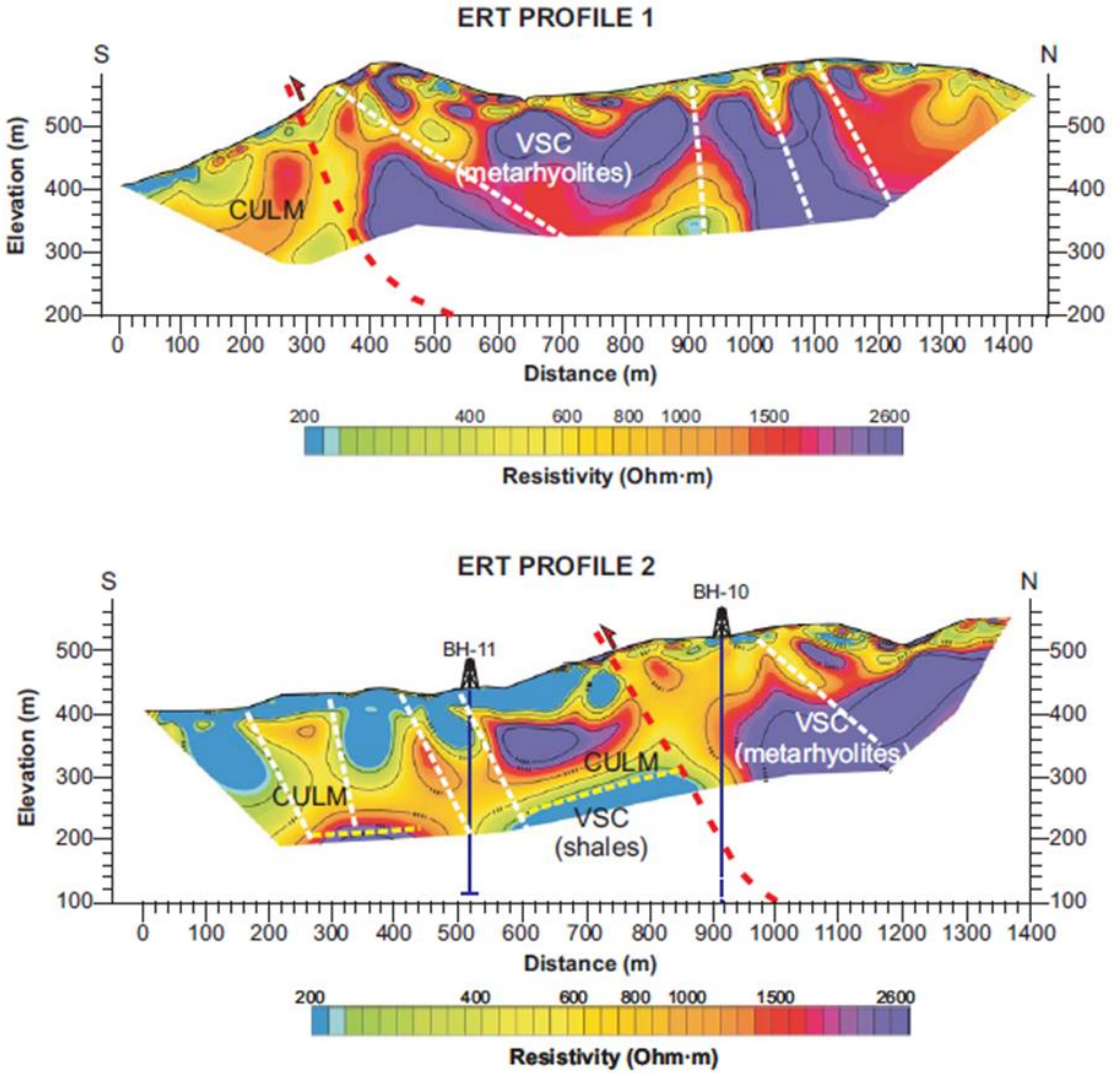


Figure S2. ERT (Electric Resistivity Tomography) sounding results for profiles 1 and 2 showing the underground lithological and tectonic structure (for more information see Gómez-Ortiz et al. (2014) Identification of the subsurface sulfide bodies responsible for acidity in Río Tinto source water, Spain. Earth and Planetary Science Letters, 391, 36–41).

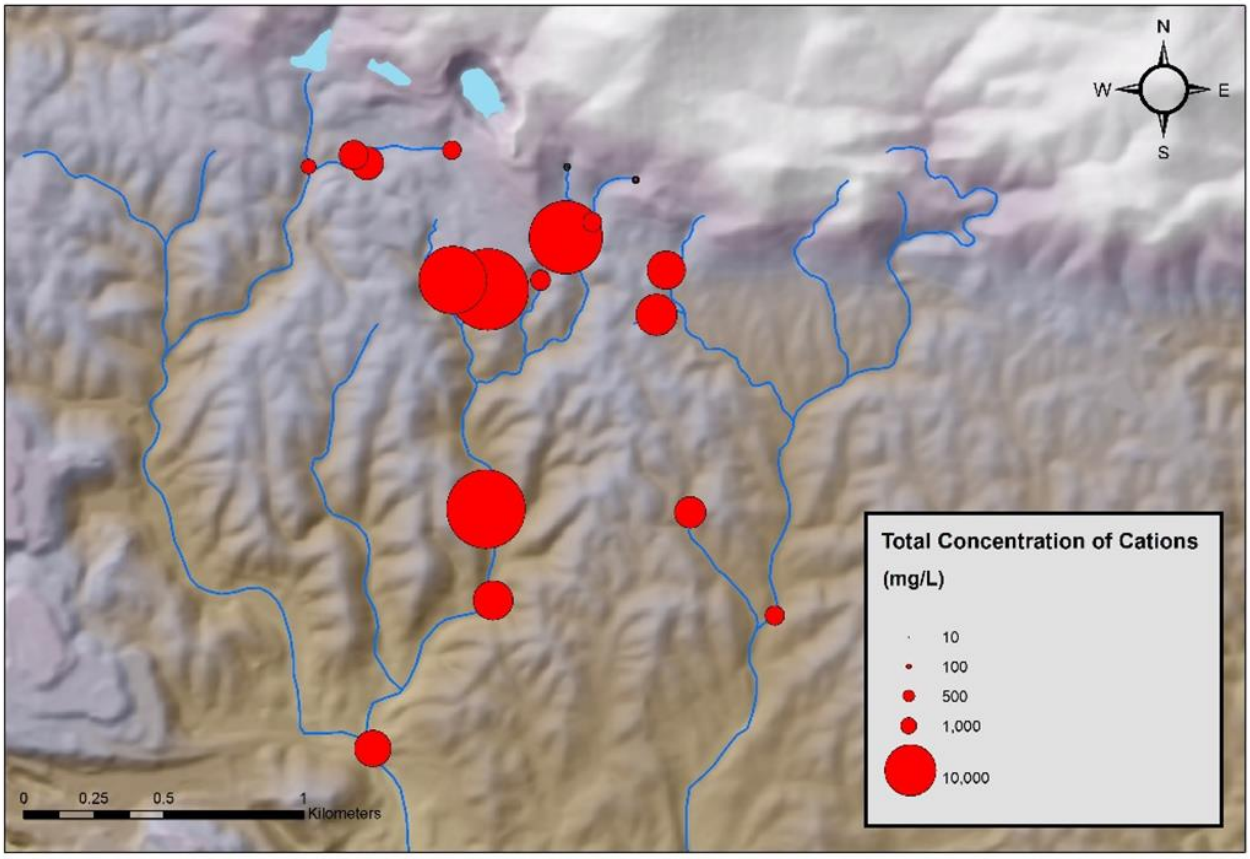


Figure S3. A GIS diagram displaying proportional symbols which represent the total cations from each of the springs.

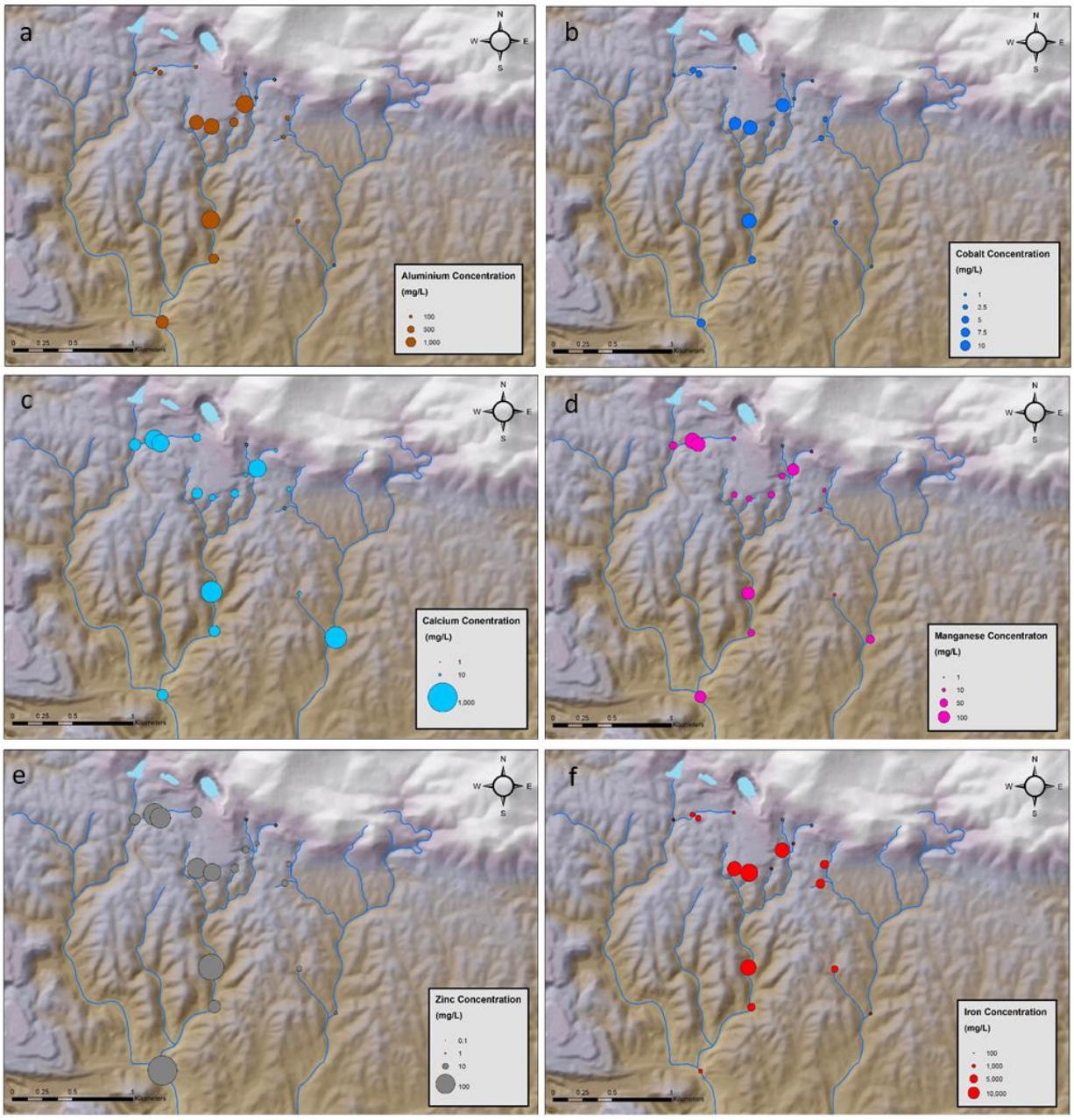


Figure S4. GIS diagram of the study area, with proportional symbols representing concentrations of specific elements in mg/L as aluminium (**a**), cobalt (**b**), calcium (**c**), manganese (**d**), zinc (**e**), and iron (**f**).

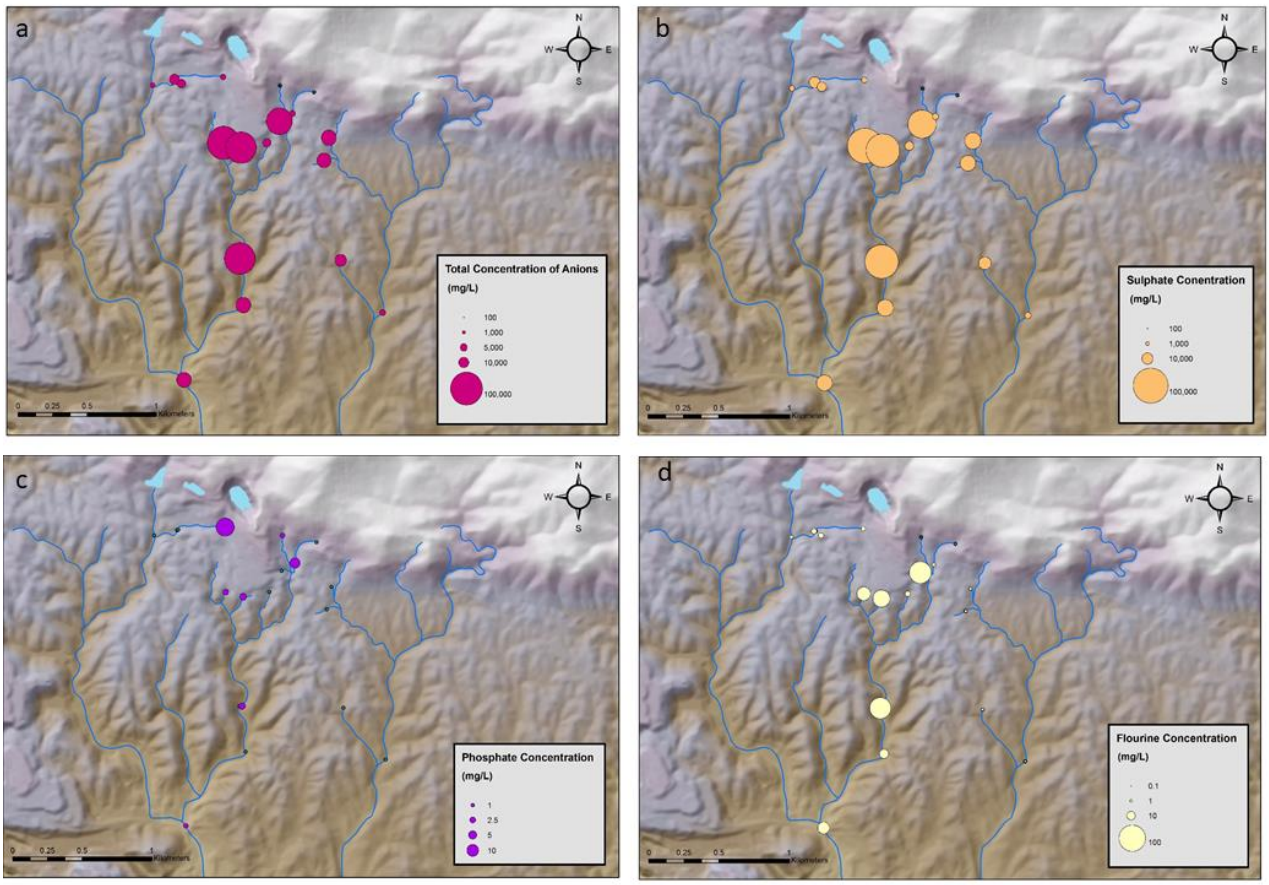


Figure S5. Different GIS maps which representing the total anion composition (**a**), Sulfate (**b**), phosphate (**c**), and fluorine (**d**) for each locality in a proportional symbology format.

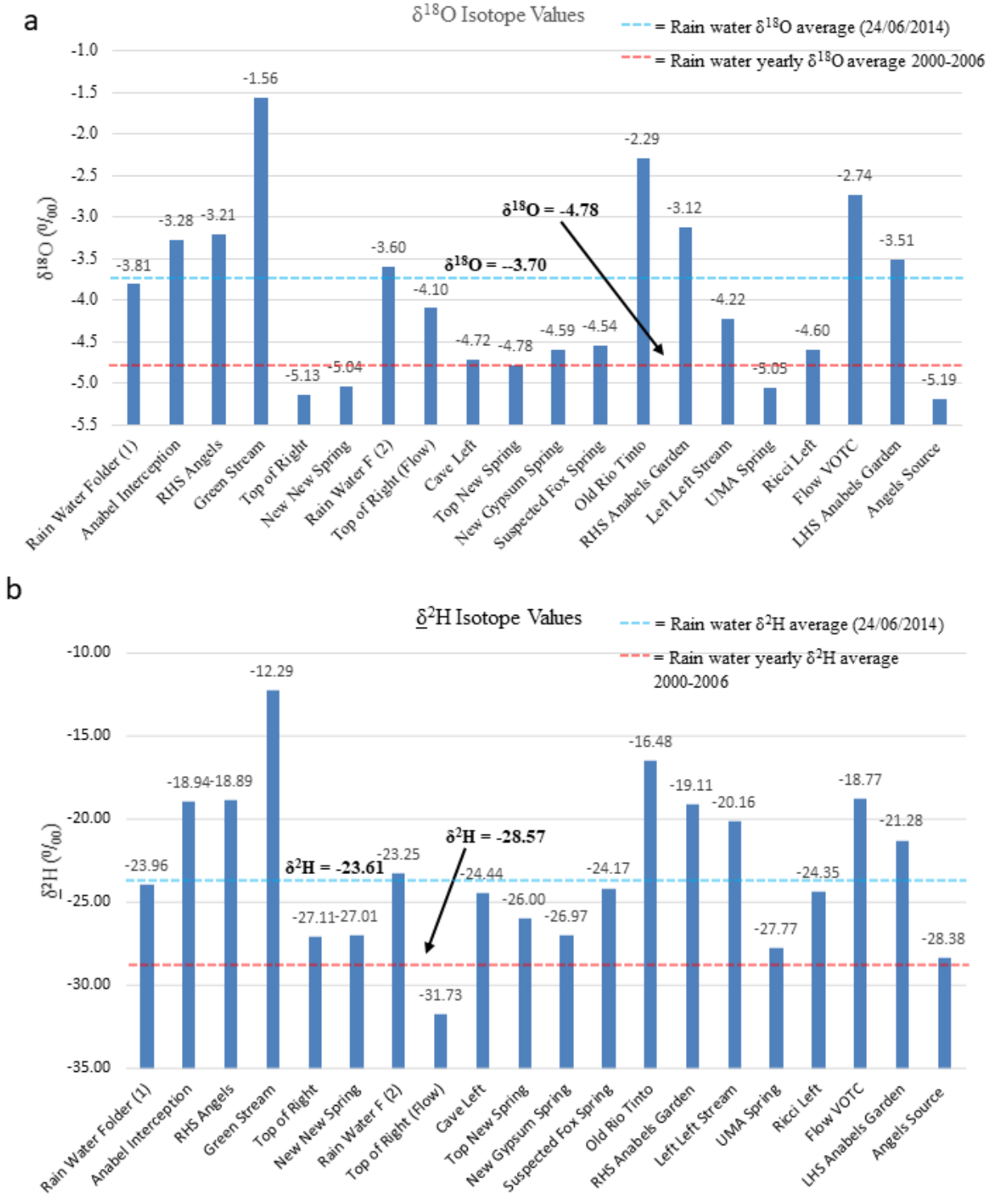


Figure S6. Rainwater and spring $\delta^{18}O$ and $\delta^{2}H$ in the study area. a) $\delta^{18}O$ values for the Rio Tinto springs, with the average $\delta^{18}O$ value for the rainwater on the 24/06/2014 and data from GNIP spanning 2000–2006; b) $\delta^{2}H$ values for the Rio Tinto springs with an average $\delta^{2}H$ value for the rain collected on the 24/06/2014 and an average of GNIP data from 2000–2006.

Table S1. Tables summarizing the accuracy of the isotopic analysis in relation to the standards, IA-RO52, IA-RO53 and IA-RO54, and the standards used in the isotopic analysis.

$\delta^{18}O$ (‰)		**Error 2σ (‰)**	**Difference (‰)**	**$\delta^{2}H$ (‰)**
Certified Value	**Measured Mean (n = 3)**			Certified Value
0.56	**0.38**	0.12	–0.18	4.93
-10.18	–**10.08**	0.07	0.10	–61.97
-19.64	–**19.69**	0.12	–0.05	–157.12

Standard	**Description**	**$\delta^{2}H$**	**$\delta^{18}O$**
IA-RO52	Low abundance natural water	–157.12	–19.64
IA-RO53	Mid abundance natural water	–61.97	–10.18
IA-RO54	Zero abundance natural water	4.93	0.56

Table S2. Rainwater average isotope data 2000-2006 for Seville. Weighted values are used to correct biases in the 2H concentration by re-evaporation processes (see Hughes, C. E. and Crawford, J. (2012). A new precipitation weighted method for determining the meteoric water line for hydrological applications demonstrated using Australian and global GNIP data. Journal of Hydrology, 464–465, 344–351. doi:https://doi.org/10.1016/j.jhydrol.2012.07.029).

Year	**Average $\delta^{2}H$**	**Average $\delta^{18}O$**	**Weighted Average $\delta^{2}H$**	**Weighted Average $\delta^{18}O$**
2000	−19.43	−4.10	−21.10	−4.53
2001	−23.62	−4.00	−27.98	−4.83
2002	−19.44	−3.64	−23.96	−4.24
2003	−32.24	−4.22	−37.55	−5.31
2004	−28.58	−4.92	−28.13	−4.97
2005	−25.74	−3.71	−26.22	−4.02
2006	−30.09	−4.90	−35.07	−5.58
Average	−25.59	−4.21	−28.57	−4.78

Table S3. Table summarizing the acid producing minerals within the VSC deposit of Rio Tinto and the acidity of each, complemented by their reaction rates through Fe^{3+} (Dold, 2010).

Mineral	Acidity generated with Fe^{3+}	Acidity generated with O_2	Mole H+/Mole per compound	Reaction rate with Fe^{3+}
Pyrite	Yes	Yes	4	$2.7 \cdot 10^{-7}$
Marcasite	Yes	Yes	4	$1.5 \cdot 10^{-7}$
Arsenopyrite	Yes	Yes	2	$1.7 \cdot 10^{-7}$
Chalcopyrite	Yes	No	2	$9.6 \cdot 10^{-9}$
Pyrrhotite	Yes	Yes	0-2	n/a

Table S4. Summarizing the PHREEQC results, with N/A assuming the mineral does not form under those conditions or that the elements are in large enough concentrations to form sufficient mineral. Standard state conditions were used within the input file.

Location	pH	Chalcedony	$Al(OH)_3$	Anhydrite	$Fe(OH)_3$	Gibbsite	Geothite	Gypsum	Hematite	Jarosite K	Melanterite	Quartz
Cave Left	3.38	-0.07	N/A	-2.57	N/A	N/A	N/A	-2.26	N/A	N/A	N/A	0.36
Left Left Stream	1.63	0.74	-9.46	-1.48	-10.61	-6.77	-4.17	-1.19	-7.41	-19.71	-0.85	1.17
Top of Right	6.38	-1.14	N/A	-2.64	N/A	N/A	N/A	N/A	N/A	N/A	N/A	-0.71
Top of Right (Flow)	5	-0.46	N/A	-0.46	-1.52	N/A	4.37	-0.16	10.75	-3.68	-2.54	-0.03
UMA Spring	1.35	0.85	-10.88	-0.53	-11.65	-8.19	-5.75	-0.24	-9.48	-21.45	-0.81	1.28
Ricci Left	2.07	0.77	-8.67	-0.82	-9.25	-5.98	-3.35	-0.53	-4.69	-16.34	-0.54	1.2
RHS Angeles	2.24	0.73	-7.34	-1.1	-10.09	-4.65	-4.26	-0.8	-6.39	-21.09	-2.76	1.16
Green Stream	2.37	0.41	-7.48	-1.24	-9.16	-7.79	-3.26	-0.94	-4.52	-18.99	-2.39	0.84
LHS Anabel's Garden	2.7	0.56	-7.16	-0.22	-8.02	-4.41	-2.11	0.09	-2.25	15.72	-1.81	0.98
RHS Anabel's Garden	1.99	0.44	-8.51	0.53	-9.9	-5.82	-4.01	-0.23	-6.01	-19.82	-1.87	0.86
Anabel Interception	2.38	0.47	-7.51	-0.9	-9.5	-4.82	-3.61	-0.6	-5.21	-20.07	-2.77	0.89
Top New Spring	1.55	0.56	-10.44	-1.16	-11.19	-7.75	-5.3	-1.17	-8.59	-21.61	-1.41	0.99
New New Spring	1.02	0.6	-11.72	-2.28	-12.63	-9.03	-6.74	-1.99	-11.46	-24.92	-1.62	1.03
Suspected Fox Spring	1.67	0.59	-10	-1.72	-10.91	-7.31	-5.02	-1.42	-8.02	-21.7	-1.62	1.02
Old Rio Tinto Conflu	2.27	0.55	-7.34	-0.71	-9.49	-4.65	-3.6	-0.41	-5.19	-18.63	-1.93	0.98
New Gypsum Spring	2.81	-0.28	N/A	-0.28	-8.16	N/A	-2.27	0.02	-2.53	-17.1	-2.61	0.02
Flow VOTC	1.76	0.57	-9.17	-0.71	-10.6	-6.48	-4.41	-0.41	-7.41	-20.51	-1.46	1
Top VOTC	1.32	1.17	-10.49	-0.01	-11.58	-7.8	-5.68	0.27	-9.35	-21.45	-0.8	1.6